Implications of the change in confinement status of a heterogeneous aquifer for scale-dependent dispersion and mass-transfer processes

D. Pedretti[a], A. Molinari[b], C. Fallico[b], S. Guzzi[b]

[a]*Earth, Ocean and Atmospheric Sciences, University of British Columbia, Vancouver BC, Canada*
[b]*Dipartimento di Ingegneria Civile, Universita' della Calabria, Rende (CS), Italy*

Abstract

A series of experimental tracer tests were performed to explore the implications of the change in the pressure status of a heterogeneous bimodal aquifer for scale-dependent dispersion and mass-transfer processes. The sandbox was filled with sands and gravel channels and patches to form an alluvial-like bimodal aquifer. We performed multiple injections of a conservative tracer from 26 different locations of the sandbox and interpreted the resulting depth-integrated breakthrough curves (BTCs) at the central pumping well to obtain a scale-dependent distribution of local and field-integrated apparent longitudinal dispersivity (respectively, α_L^{loc} and α_L^{app}). We repeated the experiments under confined (CS) and unconfined (UNS) pressure status, keeping the same heterogeneous configuration. Results showed that α_L^{loc} (associated with transport through gravel zones) was poorly influenced by the change in aquifer pressure and the presence of channels. Instead, α_L^{app} (i.e. macrodispersion) strongly increased when changing from CS to UNS. In specific, we found $\alpha_L^{app} \approx 0.03r$ for the CS and $\alpha_L^{app} \approx 0.15r$ for the UNS (being r the distance from the well). Second-to-fourth-order temporal moments showed strong spatial dependence in the UNS and no spatial dependence in the CS. These results seem consistent with a "vadose-zone-driven" kinetic mass-transfer process occurring in the UNS but not in the CS. The vadose zone enhances vertical flow due to the presence of free surface and large contrasts in hydraulic conductivity triggered by the desaturation of gravel channels nearby the pumping well. The vadose zone enhances vertical mixing between gravel and sands and generates BTC tailing. In the CS vertical mixing is negligible and anomalous transport is not observed.

Keywords: confined unconfined conditions, tracer tests, methods of moments, mixing, mass transfer, anomalous transport

1. Introduction

Understanding and quantifying the transition from local-scale to field-scale (i.e., macro) dispersion is fundamental for making accurate model-based predictions of the fate of solute plumes in heterogeneous aquifers. While local dispersion is controlled by mixing and the variation of seepage velocities at the scale of the pores (Bear, 1972), dispersion estimated from the interpretation of field-scale tracer tests becomes a scale-dependent process associated with the enhanced spreading of solute plumes by macroscopic fluctuations in hydraulic conductivity (K) (e.g., Dagan, 1989).

While the topic has received great attention in the last decades, the link between aquifer confinement status and scale-dependent dispersion has been left somewhat unexplored. Because of a variety of reasons, including seasonality in recharge patterns, use of pumping wells, earthquakes or artificial recharge practices the aquifer pressure can significantly fluctuate over time. This fluctuation can determine temporal changes in the stress state of the aquifer and generate a transition from saturated to unsaturated conditions in the aquifer (and vice-versa) (e.g., Atkinson, 1977; Simpson et al., 1989; Hare and Morse, 1997; Quilty and Roeloffs, 1997; Aish and de Smedt, 2004; Delin et al., 2007; Sayana et al., 2010; Liu et al., 2015).

The change in saturation conditions can have potential implications for the correct interpretation of plume spreading in heterogeneous settings. For instance, Pedretti et al. (2013) observed that, within a polluted DNAPL site in Italy, the direction of the hydraulic gradients rotated by 180° because of the seasonal recharge status of the local perched aquifer. This seasonal aquifer directionality affected the distribution of solute plume generated from the DNAPLs sources. Padilla et al. (1999) performed tracer tests within a homogeneous laboratory column under different saturation conditions observing that resulting breakthrough curves (BTCs) exhibit earlier initial arrival and greater tailing and variance (i.e., dispersion) under unsaturated conditions than under fully saturated conditions. The reason was associated to the decrease of the number of flow paths under unsaturated conditions, such that the velocity variation increased. van Genuchten and Wierenga (1976) showed that solute plume in variably saturated heterogeneous soils can display typical patterns associated with dual-porosity-like transport, and can be reproduced using a 1D advection-dispersion-mass transfer equation (ADMT), which is based on the classical advection dispersion equation (ADE) embedding a two-parameters kinetic term. This kinetic term can be referred to as a "memory function", where the two parameters represent a mass transfer rate coefficient and a capacity coefficient. For a review of these concepts, as well as other mass-transfer models, we refer for instance to Haggerty and Gorelick (1995).

In most applications, transport parameters are estimated through the interpretation of forced-gradient tracer tests (e.g., Ptak et al., 2004). Full mass recovering is one of the key aspects that render these tests appealing for aquifer testing compared for instance to uniform flow tracer tests, which may not ensure complete tracer recover. A drawback of forced-gradient-based methods is that closed-form formulations of scale-dependent dispersion are not easily obtained, contrasting with the large amount of existing formulations for uniform flow conditions (e.g. Gelhar and Axness, 1983; Dagan, 1984; Schulze-Makuch, 2005; Fiori et al., 2006). One difficulty is the lack of stationarity of nonuniform flow fields (Matheron, 1967), which limits the application of classical stochastic theories to forced-gradient transport. A second reason is due to the mathematical complexity of dealing with cylindrical coordinates, which are often used to estimate dispersion-related parameters under radial flow geometries (e.g., during convergent-flow tracer tests). Indeed, a very limited amount of closed-form solutions based on the 1D ADE in radial coordinates have been documented (e.g. Chen et al., 2003; Hernandez-Coronado et al., 2012). Using a spatially-variable model in a radially convergent flow setting, Chen et al. (2003) showed that the longitudinal dispersivity (α_L) scales as $\alpha_L = 4r$, where r is the distance from the extraction well. An alternative method to estimate field-scale dispersion under convergent flow conditions is through the temporal moments of a depth-integrated BTC obtained during a tracer test (e.g. Valocchi, 1986; Fernandez-Garcia et al., 2004; Pedretti and Fiori, 2013).

Molinari et al. (2015) analyzed forced-gradient tracer tests in an unconfined meter-scale heterogeneous sandbox to identify potential links among physical properties of the soil, transport connectivity indicators and the kinetic terms adopted in ADMT solution when used for upscaling purposes. The sandbox was equipped with multiple piezometers to perform multiple tracer injections around a central fully-penetrating pumping well. The experimental aquifer was characterized by a bimodal K distribution, with gravel-rich high-K layers and channels embedded in a sandy matrix. The geometrical distribution of the gravel and sand zones aimed to mimic the distribution of hydrofacies in a typical alluvial setting, where solute plumes are preferentially transported along fast-flow gravel-rich horizons and in less extent through the sandy matrix. Molinari et al. (2015) used an ADMT-like solution to satisfactorily fit the experimental BTCs, and postulated that kinetic mass-transfer-like processes could have occurred between gravel channels and the surrounding sandy matrix. In line with the previous theoretical works

(Pedretti et al., 2014), Molinari et al. (2015) suggested a physical link between aquifer connectivity and the ADMT capacity coefficient. However, no direct link was found between physical properties and the mass-transfer rate coefficient, questioning the physical validity of the ADMT solution and the actual existence of kinetic mass-transfer processes in the sandbox.

In this work, we present and discuss the results from a second investigation performed within the experimental sandbox of Molinari et al. (2015), where we focused on the implications of the different confinement status of heterogeneous aquifers on scale-dependent longitudinal dispersion and transport upscaling. Our methodology was based on two steps. First, we reinterpreted the dataset from Molinari et al. (2015), which analyzed tracer tests in an unconfined pressure status (UNS). From these data, we quantified the aquifer longitudinal dispersivity at different spatial scales using two different methods: the curve-fitting approach proposed by Sauty (1978), which provides estimates of the local spatially-invariant dispersivity (α_L^{loc}), and method of temporal moments, which provides estimates of the apparent macroscopic longitudinal dispersivity (α_L^{app}), distribution skewness and other relevant information. Then, we repeated the tracer test experiment within the same sandbox but imposing a confined pressure status (CS). We interpreted the new results from the CS using the same approach adopted for the UNS, and compared the estimated parameters against those obtained from the UNS. This comparison allowed us to quantify the impact of the change in pressure status of the aquifer with the scale-dependence behavior of longitudinal dispersivity. A conceptual numerical flow model was also developed to discuss the possible mechanisms controlling the different behavior of solute plumes in the two settings. In specific, we discuss the potential role of the pressure status of the aquifer on the development of kinetic mass-transfer processes within the sandbox.

The paper is organized as follows. In Section 2 we describe the experimental setup and provide details regarding the construction and the hydraulic configuration for each confinement setting. In Section 3, we provide the mathematical formulations adopted to analyze the BTCs and estimate local and apparent dispersivities. In Section 4, we illustrate, analyze and discuss the main results from this analysis. The paper ends with the main conclusions drawn from this analysis.

2. Experimental Setup

The experimental sandbox (Figure 1) had dimensions 144cm $\times$ 60cm $\times$ 60cm (x,y,z) and was equipped with two lateral tanks, continuously recharged to set constant head (CH) conditions at two boundaries of the box. The hydraulic connection between the sandbox and the lateral tanks was guaranteed by the presence of perforated baffles. The sandbox was equipped with twenty-six piezometers and one pumping well (Figure 1b) made by perforated pipes covered by a geotextile fabric to minimize the potential effects of well screen clogging. The central well was equipped with a ball valve to control the outlet rate from the system and define a proper pumping flow rate (Q)

during the tests. The piezometers (pzs) and the pumping well have one and three cm diameter, respectively, and are fully penetrating the aquifer.

The sandbox was filled with a fairly homogeneous sand and embedded by clean gravels, forming channels and blocks. The grain-size distribution (GSD) of the two materials is reported as Supplementary Material, together with the distribution of the silty material employed to create a confined pressure system (described below). There was no silty or clayey material within the original aquifer created by Molinari et al. (2015). The saturated hydraulic conductivity of gravels and sands was determined from permeability tests (Mariotte bottle). We obtained $K = 10^1 - 10^2$ m/d for the gravels and $K = 5 \times 10^{-2} - 10^{-1}$ m/d for the sands.

For each flow configuration, we performed a series of pulse injections of a conservative tracer (potassium iodide) from the different piezometers, which acted as injection locations. In each piezometer we injected a concentration of 3×10^{-3} M, through a volume of the injected mass equal to 10 mL, by means of a syringe and ensuring well-mixed conditions within the well. In each piezometer, the injection took place in the order of a few seconds. We measured the resulting depth-integrated BTCs at the central pumping well, under quasi-steady flow conditions. A data logger, connected to an electrical sensor, was placed in a measurement tank collecting the pumped water. By means of a previous calibration, we converted the resulting measured voltage to the salt dissolved concentrations. To avoid overlapping the results from each multiple injection location, before each new injection we ensured that the entire mass from the previous experiment was entirely collected from the pumping well.

2.1. Unconfined Setting (UNS)

The UNS by Molinari et al. (2015) was generated as follows. At the bottom of the box, a first 20-cm-thick stratum of pebbly sand was placed. On top of this stratum, a first 3-cm-thick heterogeneous layer (Layer 1) was created and filled with gravel channels and blocks surrounded by sand (Figure 1c). The resulting arrangement of gravel materials in Layer 1 is conceptually shown in Figure 1d. A 156 cm long channel crosses the system from the top-left corner of the box to the opposite bottom-right one. It intercepts the pumping well and it is located close to pz 3I, 1C, 1B. The second channel has a length of about 50 cm with the extreme edge placed between pz 3C and 3D. The gravel block has planar size 28 cm $\times$ 7 cm and it is located on the left side of the domain intercepting pz 1H and 2H.

Layer 1 was then covered by a 15 cm thick stratum of sand. On top of this sand, a second 3-cm-thick heterogeneous layer (Layer 2) was created and filled with gravel channels and blocks with a sandy matrix (Figure 1e). The resulting arrangement of gravel materials in Layer 2 is conceptually shown in Figure 1f. This layer is also characterized by two gravel channels and one gravel block, as in Layer 1 but with a different spatial arrangement. One channel, with a length of about 96 cm, extends from the top-left corner of the box to the central-bottom leaning against pz 3I and 1F. The second channel intersects, in correspondence of pz 2G, the other gravel channel. It has a length of about 123 cm and leans against pz 1I, 3E and 3D. Within Layer 2 the gravel block is located in the center of the right side of the box surrounded by sand. Layer 2 was then covered by a 10-cm-thick stratum of sand to obtain an overall aquifer thickness of 51 cm.

To generate unconfined flow conditions, we imposed a constant pumping rate equal to $Q = 5 \times 10^{-2}$ L/s and set the hydraulic head (h) boundary to h=45cm (from the bottom of the box). This setup recreated unsaturated conditions above the water table, which had an elliptical-like shape around the pumping well. Around the well, the head levels dropped to $h \approx 37$ cm, i.e. slightly less than 25% of their initial values. For this reason, Molinari et al. (2015) assumed that the aquifer system could be evaluated as an equivalent confined one, under the limit of validity of the Boussinesq approximation (Bear, 1979). Nonetheless, in the proximity of the pumping well the drawdown created unsaturated conditions within Layer 2, which is located at an elevation between z=38cm and z=41cm. This issue is highlighted as a key aspect for the interpretation of our results.

2.2. Confined Setting (CS)

In natural alluvial settings, confined aquifer conditions are generally associated with the presence of low-permeable materials (confining units), such as clayey or silty caps. The head levels can exceed the aquifer top elevation, generating positive pressures. To obtain CS, we modified the original UNS by removing the top 5 cm of sands (above Layer 2) and replaced them with a 5 cm thick silty layer with clay and fine sands. Then, we raised the head levels of the lateral boundaries to h=52cm, such that the new configuration was completely saturated under unpumped conditions. Under pumping conditions, using the same Q employed for the UNS, we did not observe the development of localized unsaturated conditions. This includes Layer 2 in proximity of the pumping well, which was unsaturated during the execution of the tracer tests in the UNS.

3. Estimation of dispersivity

Two different methodologies were adopted to provide estimates of longitudinal dispersivity at local and field scales. The first methodology is based on curve-type matching using the solution by Sauty (1978). This approach provides a measurement of the local scale-invariant longitudinal dispersivity (α_L^{loc}) associated with the position of the injection location. The second methodology is based on the method of temporal moments and corrected for forced-gradient convergent flow geometries, following Fernandez-Garcia et al. (2004). This solution provides a measurement of field-scale apparent longitudinal dispersivity (α_L^{app}). The results in the two estimated dispersivities and for each confinement setting (UNS and CS) are analyzed and discussed in Section 4.

It is noted that the potential influence of the piezometers on the flow field and transport dynamics is not explicitly accounted for. Despite the piezometer diameter (1cm) being somewhat wide considering the lateral extension of the sandbox (144cm × 60cm), we corroborated via modelling analysis -not reported here- that neglecting the presence of the piezometers has little influence on the flow and transport dynamics within the box and therefore does not qualitatively affect our conclusions. This modeling exercise also suggests that diffusion (e.g., Rolle et al., 2013) can be neglected from these calculations, likely due to the advection-dominated transport within the sandbox.

3.1. Local dispersivity (α_L^{loc})

The approach is based on a curve-fitting of a set of theoretical curves representing the analytical solution of the ADE for different parameters and for initial and boundary conditions similar to those used in our analysis. The method was developed initially by Sauty (1978), who assumed cylindrical flow conditions in an isotropic homogeneous 1D aquifer. The governing equation for a conservative tracer and no sink/sources in an advection-dominated system can be written as

$$\phi\frac{\partial C}{\partial t} = q\frac{\partial C}{\partial r} + \frac{1}{r}\frac{\partial}{\partial r}\phi D_L^{loc}\frac{\partial^2 C}{\partial r'^2} \tag{1}$$

where ϕ is the porosity [-], C the concentration [mol/L], t is the time [s], q is the average pore velocity and D_L^{loc} is the coefficient of longitudinal hydrodynamic dispersion [m^2/s], approximated as $D_L^{loc} = \alpha_L^{loc}|q|$. The units of r and α_L^{loc} are [m]. In the original Sauty's approach, $q = \phi A/r$, being $A = Q/(2\pi r b\phi)$, where b [cm] is the aquifer thickness. The analytical solution of (1) for a pulse injection of a tracer becomes

$$C_D = \frac{K'}{t_D^{3/2}} \exp\left[-\frac{r(1-t_D)^2}{4\alpha_L^{loc} t_D}\right] \tag{2}$$

where $C_D = C/C_{\max}$, $C_{\max}$ is the maximum concentration, $t_D = r/q$ and K' is a dimensionless amount defined as

$$K' = t_D^{3/2} \exp\left[\frac{r(1-t_{\max})^2}{4\alpha_L^{loc}}\right] \tag{3}$$

where

$$t_{\max} = \left[1 + \left(\frac{3\alpha_L^{loc}}{r}\right)^2\right]^{1/2} - \frac{3\alpha_L^{loc}}{r} \tag{4}$$

The parameter α_L^{loc} is estimated by matching the experimental BTC with a set of theoretical curves associated with fixed values of the ratio r/α_L^{loc}. An optimization procedure based on minimization of the quadratic errors between observed curves and curve type was followed to determine the best r/α_L^{loc} ratios. Additional details regarding the estimation process can be found in the Supplementary Material. Despite the Sauty's approach being widely adopted for the parameter estimation, this method is based on a 1D ADE with a local dispersivity term and no mass transfer, which undermines its actual validity to reproduce the strongly nonsymmetric BTCs typically observed in heterogeneous aquifers. In specific, Molinari et al. (2015) noted that the 1D ADE was able to fit satisfactorily the rising limb of the BTCs from the UNS, which is associated with the early-arrival time of solute particles at the control section and thus corresponds to local dispersivity of gravel-rich "mobile" zones of the aquifer. Based on this observation, α_L^{loc} was estimated from the rising limb of the BTCs. We discuss the implication of this selection in the next section.

The sandbox boundary conditions generate an elliptical flow field within our artificial system and this condition prevent the direct application of the original Sauty solution, which is exact for cylindrical conditions. To circumvent this limitation, for each aquifer setting we calculate $t_D = t/t_A$, in which t_A is the advective time of a tracer injected in an equivalent homogeneous 2D medium characterized by $K = 10^1$ m/d (i.e., the minimum K estimated for the gravel sandbox) with geometry and boundary conditions similar to the sandbox. The advective time is calculated using a numerical groundwater flow model and a particle-tracking algorithm. The methodology is described in detail in Molinari et al. (2015) to which we refer for further information.

3.2. Field-scale apparent dispersion α_L^{app}

The method of temporal moments develops from the original analysis by Aris (1956), and it was used to obtain field-scale apparent transport parameters (Fernandez-Garcia et al., 2004). Apparent parameters are used in local ADE formulations to obtain the same temporal moments as observed in the field. Valocchi (1986) showed that these moments can be easily derived from the calculation of solute arrival time at a control plane in Laplace space under radial convergent transport conditions. Fernandez-Garcia et al. (2004) followed this approach to obtain an estimation of the field-scale dispersion from experimental BTC obtained during convergent flow tracer tests. The first temporal absolute moment of the BTC can be defined as

$$\mu_1 = \frac{\int_0^\infty tC(t)\mathrm{d}t}{\int_0^\infty C(t)\mathrm{d}t} \tag{5}$$

and represents the time scaling of the mean arrival time of the solute at the control plane (i.e., the pumping well). Using (5), the n-th central temporal moment can be written as

$$\mu_n = \frac{\int_0^\infty (t-\mu_1)^n C(t)\mathrm{d}t}{\int_0^\infty C(t)\mathrm{d}t}. \tag{6}$$

The second moment (μ_2') can be interpreted as the variance of the solute particles travel time arriving at the depth-integrated well over time. Under uniform flow, it holds that

$$\alpha_L^{app} = \frac{r\mu_2}{2\mu_1^2} \tag{7}$$

Eq. (7) can be used to obtain an estimate of α_L^{app} for each injection location, which can be directly compared with the estimations obtained from the Sauty solution. Fernandez-Garcia et al. (2004) noted that, for advective dominated transport, Eq. (7) can overestimate the dispersivity with respect to the one derived from a radial flow tracer test by a factor 4/3. Despite the flow configuration within our box deviating from a radial-like condition, we adopted a conservative approach and corrected our results based on this factor. It is highlighted that this approximation equally affects the results for both CS and UNS and thus it does not qualitatively affect our main conclusions.

4. Results and analysis

4.1. Results

Figure 2 illustrates the scale-dependent behavior of α_L^{loc} and α_L^{app} for each confinement setting analyzed. Both dispersivities and injection distances are plotted in meters. As in Chen et al. (2003) , we adopted a linear regression function of the form $\alpha_L = mr$, from which the angular coefficient m helps to quantify the scale dependence of the dispersivity. The complete list of BTCs is reported as Supplementary Material. We experienced some technical problems during the execution of the tests and data post-processing and a few BTCs were not available for the analysis.

Local dispersivity behaves quite similarly in both UNS and CS. The range of the estimated values is in the order of $\alpha_L^{loc} \approx 10^{-2}$m, which is smaller than the *rule-of-thumb* $\alpha_L \approx 0.1L$ usually adopted for sandy aquifers (L being the domain size). This value is more similar to local dispersivity of coarse-textured soils, such as clean gravels, in which the solute samples less tortuosity than in sandy aquifers and thus reduces the effects of pore-scale mixing. Being α_L^{loc} estimated from the rising limb of the BTC, this result suggests that the early arrival time of the plume is controlled by the presence of preferential flow gravel-rich zones in the sandbox. This is true for both confinement status and indicates that the mechanisms controlling local dispersion in the gravel horizons are similar in the two settings. The estimated α_L^{loc} are also consistent with the modeled values by Molinari et al. (2015). The limited growth of α_L^{loc} with the injection distance is similar in the two confinement settings and characterized by $m \approx 0.01$. This observation suggests that the local dispersivity is quite independent from the injection-extraction distance and from the type of confinement. Thus, α_L^{loc} (being estimated from the rising limb of the BTC) does not provide any information about the presence of heterogeneity. The results are instead consistent with the findings by Saffman (1960), who suggested that at small scales the dispersivity should be correlated with the grain size and not necessarily with the dimension of the system.

The scale-dependent behavior of α_L^{app} is more striking and highlights clear differences between the two settings. We observe $m \approx 0.03$ for the CS and $m \approx 0.15$ for the UNS. Defining the ratio between field-scale (i.e. apparent) and local scaling coefficients as $\lambda = m_{app}/m_{loc}$, we obtain $\lambda_{CS} \approx 3.23$ for the CS, and in $\lambda_{UNS} \approx 14.53$ for the UNS.

In the CS, $\lambda_{CS} \approx 3.23$ is consistent with the scaling factor 4 by Chen et al. (2003), obtained using a scale-dependent dispersivity model. Indeed, the method of moments can also be seen as scale-dependent approach, since the method integrates the fluctuation of travel times occurring at all transport scales when travelling in the heterogeneous box, and not only associated with transport in the fast-flow zones. We also observed that, in the CS, local and apparent dispersivity exhibit comparable values ($\alpha_L^{app} \to \alpha_L^{loc}$) as $r \to 0$ and (consistently) both scale as $\alpha_L^{app} \approx 10^{-2}$m. Expressed in words, this means that at short travel distances the dispersion becomes controlled by local mixing processes and not by the dynamic effect of the heterogeneous velocity field.

In the UNS, $\lambda_{UNS} \approx 14.53$ largely overestimates the scaling factor found by Chen et al. (2003), suggesting that the scale dependence of macrodispersion in the unconfined setting is enhanced compared with macrodispersion in the confined setting. We now note that $\alpha_L^{app} \approx 0.1r$ is more consistent with the *rule-of-thumb* behavior for sandy systems. As $r \to 0$, the apparent dispersivity in the UNS is still 10 times larger than in the CS and does not reduce to the local dispersivity associated with gravel. For instance, at $r \approx 0.15$ m, we found $\alpha_L^{app} \approx 0.02$ m, which is in line with the estimated local longitudinal dispersivity for the sandy matrix obtained by Molinari et al. (2015).

We further investigated whether the analysis of higher temporal moments could provide additional insights regarding the scale dependence of BTC statistics, in addition to dispersivity. The results are shown in Figure 3, where the normalized third and fourth moments are calculated as

$$\mu_n' = \frac{\mu_n}{\mu_1^{n-1}} \tag{8}$$

where μ_n is calculated as in Eq. (6). The results indicate that in the UNS there is a marked scale dependence of the two moments, which is similar to the spatial behavior of the dispersivity. A positive increase in the third moment, in specific, indicate an increase in tailing of the BTC with space, suggesting that the non-Fickian behavior is continuously evolving in the system. This result clearly indicates lack of ergodic behavior of transport in the UNS domain. On the contrary, CS higher moments are very close to zero, which indicate a high degree of symmetry of these curves. This is true for any injection point from the aquifer.

Overall, the greater dispersion and skewness found from tracer tests in the UNS compared with tracer tests in the CS suggest that transport in the UNS may be influenced by specific mixing and spreading mechanisms which are less pronounced in the CS. More precisely, in the CS it is likely that dispersive mechanisms may be mainly controlled by local mixing through gravel, showing less scale dependence. This behavior is somewhat unexpected for this bimodal aquifer and the tracer test setup. Despite the aquifer being largely dominated by sands, the tracer should enter the aquifer in a flux-weighted mode through the piezometers. Thus, independently from the confinement setting, the majority of the mass should migrate preferentially along the heterogeneous high-K channels and to a less extent through the sandy matrix. Hence, it could be expected that UNS and CS show a similar dispersion. A possible explanation of the difference between UNS and CS is proposed in the following section, and accounts for the different saturation conditions in the two systems and the resulting implication for solute advective mechanisms in variably saturated media.

4.2. Interpretation

In the CS, the system was fully saturated during the test and in pressurized status. In the UNS, the system went below saturation in specific zones of the aquifer and the water suction (ψ) became locally positive, including parts of Layer 2 close the pumping well. Under unsaturated conditions, it is well known that the hydraulic conductivity becomes a function of the suction, i.e., $K(\psi)$. More specifically, K decreases as ψ increases. The reduction in K is much more pronounced in gravel soils, which have a much lower air-entry pressure than finer soil. If a specific ψ threshold is exceeded, the relative hydraulic conductivity of gravel soils can be lower than the relative hydraulic conductivity of sandy soils (e.g., Woesten and van Genuchten, 1988). Thus, water may flow preferentially through sandy layers than in gravel layers. In turn, this implies that solute may also preferentially travel through the sandy matrix under unsaturated conditions.

We assessed the potential relevance of this effect on our experiment by simulating a 2D unsaturated flow velocity field representing a conceptual vertical slice of the sandbox. We adopt the finite elements code SEEP/W (GEO-SLOPE, 2006), which has been successfully used in a variety of variably-saturated flow problems (e.g., Motha and Wigham, 1995; Hughes et al., 1998; Chesnaux, 2009; Masetti et al., 2010, 2015). We assumed for simplicity that the lateral extension of gravel-rich zones is continuous within each layer, in order to stress the relative importance of saturation conditions in our system. The model is illustrated in Figure 3. The problem is solved considering an axial-symmetric geometry and run in steady state. The system is discretized into quadrangular elements of regular size 1cm $\times$ 1cm. The boundary conditions and geometrical distribution of the layers replicate those of the real sandbox. In specific, we simulate the well by imposing a constant volumetric discharge (same as Q) at the basal element of the side opposite to the constant-head boundary conditions, and set high vertical anisotropy to the conductivity of the elements of the corresponding well column (black elements in Figure 3). In this sense, the partitioning of discharge rates among different aquifer layers within the well column is not deterministically imposed but calculated by the code. The material properties are estimated from the experimental GSDs. The soil-water characteristic curve (SWCC) is obtained using the Arya and Paris (1981) method. The $K(\psi)$ function is estimated using these SWCC through the Green and Corey (1971) solution. Both methods are native function in SEEP/W. Volumetric water content at saturation and saturated hydraulic conductivities are the same as those obtained in the experimental sandbox characterization. The resulting SWCC and $K(\psi)$ functions are reported in the Supplementary Material.

Figure 4 shows the relative magnitude of the vertical and horizontal components of the flow velocity field in the two settings. In the CS, flow is primarily horizontal and dominated by the high-K channels. The vertical velocity is approximately two orders of magnitude slower than the horizontal velocity. This is true for both Layer 1 and Layer 2. Hence, solute particles being injected at any vertical plane between the constant-head boundary and the pumping well would enter in the CS preferentially through the two high-K layers, and being transported towards the well without interfering with the sandy matrix (i.e., as in a perfectly stratified system).

In the UNS, the presence of the unsaturated zone generates a different flow configuration and two different effects can simultaneously overlap. First, the UNS has a free surface which generates a distorted flow net, resulting in non-zero vertical velocity components. Second, we shall consider that, farther away from the well, horizontal flow component largely dominates over the vertical flow component. Solute particles being injected at a vertical plane away from the pumping well would mainly enter the UNS through the two high-K (locally saturated) layers, as well as in the CS. As the injection plane approaches the well, however, the flow anisotropy in the UNS decreases and the vertical flow components become increasingly important. In the proximity of the well, the vertical flow component in Layer 2 dominates over the horizontal flow component. This occurs specifically at the point highlighted by an arrow in Figure 4, and corresponds to the zone where the water table crosses Layer 2. Between this point and the well, Layer 2 becomes unsaturated, and its relative hydraulic conductivity drops below the hydraulic conductivity of the underlying sands, which remains saturated. This causes the water to preferentially move downwards instead of crossing the water table and remaining with the gravel zones.

This simple flow model helps to analyze the mechanisms controlling the additional scale-dependent apparent dispersion in the UNS compared to CS. From one side, the presence of the unsaturated zone in the UNS enhance vertical mixing between gravel and sandy aquifer, compared to the CS. From the other side, the flux-weighted partition of solute injection between gravel and sand zones in the UNS is not as sharp as in the CS, such that the injected mass can more easily enter in the two systems through the sandy matrix. We conceptually illustrated these aspects in Figure 5-top. In the UNS, the portion of the solute travelling along Layer 2 may have been transferred from the gravel channels to the sandy matrix, as the plume approached the interface between saturated and unsaturated domains in proximity of the well.

The resulting "vadose-zone-driven" mass-transfer process from the gravel to the sands with the UNS is inherently kinetic, since it is controlled by (a) the increasing vertical flow components of the gravel layer as $r \to 0$, and (b) the transient arrival time of the solutes moving toward the zone where mass transfer occurs, and (c) the presence of the free surface. Furthermore, part of the solutes may also enter the system through the sandy matrix and travels at slower rates than in gravel zones, generating a bimodal scaling of the observed BTCs. The CS does not seem to show these mechanisms. Gravel-to-sand mass transfer do not occur due to the horizontal nature of flow within the high-K layers, while a limited amount of mass enters the aquifer and travel through the sands. In addition, no free surface occurs in the CS, such that the flow lines are generally subhorizontal and vertical mixing is limited or negligible within the confined system.

5. Discussion: implication for upscaling

We discuss the potential implications of the mechanisms controlling transport upscaling in the two confinement systems and their link with the variable pressure status of the aquifer. We first consider that in the UNS, for the same injection locations, the BTCs display enhanced anomalous behavior than those performed within the CS. As an illustrative example, Figure 5-bottom shows the BTCs obtained from injection location 2I. The UNS curve is more nonsymmetric than the corresponding CS, with a steep rising limb and a long descending limb with pronounced *tailing* (Giddings, 1963). On the other hand, the BTCs in the CS showed a more symmetric distribution of concentrations, with gradients of the rising limb comparable with those of the descending limb. In both UNS and CS the curves are double peaked. In the UNS, a first peak scales at a comparable time with the two peaks of the corresponding BTC observed in the CS. This time corresponds roughly correspond to the characteristic advection time of the gravels, according to Molinari et al. (2015).

Our box is hydraulically bimodal, and as it occurs in many hydrogeological settings such as soils, alluvial systems or fracture aquifers, BTCs are often amenable to be upscaled using an ADMT model (e.g., Coppola et al., 2009; Pedretti et al., 2014; Joshi et al., 2015; Zhang et al., 2015; Vishal and

Leung, 2015). Simple 1D ADE solutions without mass transfer term are not able to provide a good fitting on nonsymmetric BTCs. For illustrative purposes, we report in Figure 5-bottom the fitted models with and without mass transfer models for a representative injection location in the sandbox (pz 2I). The UNS curve was already obtained by Molinari et al. (2015), who showed that the ADMT solution accurately reproduced the observed BTC. The same model without mass transfer (i.e. the 1D ADE) was not able to fit the UNS BTCs. Here, we show that the 1D ADE model is indeed able to fit the CS curve. We also found that the ADE model also satisfactorily fits the other experimental curves from the CS, with low RMSE and large R^2 coefficients (Supplementary Material), further supporting the hypothesis that no mass transfer is occurring in the CS. Details regarding the implementation of the CS fitting model are also reported in the Supplementary Material.

Mass-transfer-based solutions are often criticized because in some cases there is no direct correlation between the fitted mass-transfer parameters and the physical properties of the heterogeneous aquifer. This fact strongly limits the use of these solutions for predictive purpose (e.g. Neuman and Tartakovsky, 2009; Fiori et al., 2015). The proposed conceptual model may explain that kinetic mass-transfer mechanisms can be actually physically occurring in the box. In the UNS, the combined effect of free surface and the unsaturated portion of the gravels enhance vertical mass exchange by ”forcing” solute to move from the gravel (where they preferentially entered the domain) to the sand. Due to the convergent nature of flow to the well, the rate at which this mass exchange occurs is expected not to be equivalent in all contact points between gravel zones and the sandy matrix. Rather, it is expected to be higher in the proximity of the well and lower elsewhere. The non-uniform nature of the flow system supports the validity of a kinetic mass-transfer-based 1D solutions to upscale this aquifer. In specific, the additional mass-transfer term in the ADE formulation plays the role of a supplementary kinetic mixing mechanism between preferential zones and sandy matrix. This process is not embedded in 1D ADE formulations without mass transfer terms, thus limiting the ability of this solution to fit the observed curves in the UNS, as explained in Molinari et al. (2015). Yet, it works to describe the CS because under confined conditions vertical flow and related vertical mixing mechanisms are negligible.

In our analysis, tailing is primarily assumed to be a macroscopic effect of the additional vertical transport mechanisms found in UNS. Contrarily to transport under uniform flow condition, horizontal transversal mixing is expected to play a secondary role in the box. Indeed, under forced-gradient convergent flow conditions and in the proximity of a depth-integrated pumping well the aquifer dynamics are dominated by a strong pumping-driven flow component that tends to laterally drag solutes towards the well. In an analysis by Pedretti et al. (2013), for instance, it was observed that BTCs found from the 3D simulations in heterogeneous multigaussian systems showed pronounced tailing, while 2D simulations reproducing horizontal transport along each plane composing the 3D simulations (and having the same local horizontal transversal dispersivity as 3D counterparts) did not generate tailing. The 2D simulations were found quite symmetric, as if horizontal mixing had very small influence on the arrival time of the injected particles. On the other hand, vertical dispersion had a much stronger implication on tailing from the 3D BTC and controlled the mixing processes between the different layers composing the heterogeneous aquifer. The analysis by Pedretti et al. (2013) is quite consistent with the findings from the experimental box presented here. Layering (or transport stratification) is emphasized under convergent flow conditions, compared to uniform flow conditions, because of the intrinsic nature of forced-gradient transport. This also explains why simple analytical solution of vertically stratified models are able to reproduce tailing under convergent flow settings (Pedretti and Fiori, 2013).

We finally highlight that from the visual inspection of the experimental BTCs (Supplementary Material) anomalous early-time arrival of the contaminants can provide an additional perspective regarding the role of connected features and variably confined pressure status of an aquifer. The implication of early-time solute breakthrough is left open for a future investigation and analysis, as it may require a different type of modeling approaches, including for instance a fully calibrated 3D ADE model or a nonlocal radial fractional ADE model (e.g., Benson et al., 2004) to be properly addressed.

6. Conclusions

The fluctuation of hydraulic heads in heterogeneous aquifers can determine variability in aquifer pressure status, with consequences for solute transport. Within our study, we explored the impact of these fluctuations on scale-dependent dispersion in a bimodal sandbox where gravel channels are embedded in a sandy matrix. Without changing the geometrical distribution of heterogeneous channels, we imposed different constant head conditions to recreate confined and unconfined aquifer status. In each pressure status, a series of forced-gradient tracer tests was performed from 26 piezometers to obtain a scale-dependent distribution of local (α_L^{loc}) and field-integrated apparent (α_L^{app}) dispersivities.

The results showed that the change in aquifer pressure significantly affects scale-dependent dispersion. Adopting a linear regression function, of the form $\alpha_L = mr$, to identify the correlation between the estimated dispersion and the scale of observation (r), we found that:

- in both unconfined and confined setting, the local dispersion (associated with transport through preferential gravel zones) was found $\alpha_L^{loc} \approx 10^{-2}r$, consistent with the fact that α_L^{loc} is associated with local mixing and is insensitive to the presence of macroscopic K heterogeneity;

- in the confined setting, field-integrated dispersion grows at a rate $\alpha_L^{app} \approx 0.03r$, which is consistent with the scaling factor reported in a previous analysis by Chen et al. (2003);

- in the unconfined setting, field-integrated dispersion grows at a rate $\alpha_L^{app} \approx 0.15r$, i.e. about five times larger than the corresponding confined aquifer.

The larger scaling factor observed under unconfined conditions highlighted that additional dispersive mechanisms can develop under this pressure configuration while under a confined pressure status the same mechanisms do not seem to develop or at least play a negligible role on the overall transport dynamics. These considerations are in agreement with the following conceptual model:

- the drawdown (caused by the pumping well) in the unsaturated setting results in localized unsaturated conditions within the gravel channels;

- a lower unsaturated hydraulic conductivity characterize these gravel units compared with the (still saturated) conductivity characterizing the underlying sands;

- this condition forces mass transfer to occur from the gravel channels to the sandy material, causing additional mixing and dispersion.

This conceptual model is supported by a numerical simulation reproducing unsaturated flow conditions in a vertical slice of the aquifer. It also provide an explanation for the enhanced anomalous behavior of breakthrough curves in the unsaturated domain, compared to the analogous curves obtained from injections in the fully saturated system.

Our study indicates that the transient variability of the aquifer pressure status (associated for instance with the temporal fluctuation of hydraulic heads) in heterogeneous aquifers can control the scale-dependent dispersion of solute pollutant. Therefore, it needs to be accounted for when properly interpreting macrodispersion processes and obtaining effective solute transport parameters in heterogeneous settings. This includes the accurate interpretation of mechanisms controlling mass-transfer processes from fast-flow channels into a less-permeable matrix, which is generally adopted as a conceptual model for effective nonequilibrium-based upscaling solutions.

Acknowledgements

The authors are indebted with Prof. Daniel Fernandez-Garcia (UPC - Barcelona Tech), who provided logistic support to perform the tracer tests and fundamental hints for the accurate interpretation of our results. We acknowledge the comments and suggestions from the three anonymous reviewers that helped to significatively improve the quality of our manuscript.

Figures Captions

Figure 1: (a) Front view of the sandbox during dismantling operations; (b) distribution of the piezometers and the central well in the box; (c) aerial view of the box during construction of Layer 1; (d) resulting arrangement of gravel materials in Layer 1; (e) aerial view of the box during construction of Layer 2; (f) resulting arrangement of gravel materials in Layer 2. At the bottom, schematic vertical section of the box in the two settings (i.e., UNS and CS). Note the presence of silty material in the CS, shown in grey color.

Figure 2: Estimated local (α_L^{loc}) and apparent (α_L^{app}) longitudinal dispersivity in the aquifer versus the radial distance (r) of the injection well from the pumping well. The best-fitted curves (dashed lines) for UNS and CS are respectively shown in red and blue together with the corresponding m value. For Sauty's local dispersivity, $m = 0.01$ fits both CS and UNS. The curve with $m = 0.04$ (green) is similar to the expected scaling according to Chen et al. (2003).

Figure 3: Spatial dependence of the normalized third and fourth temporal moments versus the radial distance (r) of the injection well from the pumping well. The dashed lines are shown for illustrative purposes and have regression coefficients m similar to the behavior of the dispersivity in the two settings.

Figure 4: Numerical simulation of saturated-unsaturated flow velocities in two synthetic aquifers with geometrical distribution and hydraulic properties of gravel-rich layers and sandy matrix similar to the experimental box. Note that the scale of the velocity field is the same for the four resulting maps, and emphasizes the strong vertical flow component in the UNS compared with the CS.

Figure 5: (top) Proposed conceptual model explaining the additional dispersion in the aquifer associated with the presence of unsaturated zones in the gravel-rich layer L2. (bottom) Comparison of BTCs obtained after injecting at pz 2I in the two different confining settings. The BTCs were fitted by the effective 1D bimodal model embedding a mass-transfer term (Molinari et al., 2015).

References

References

Aish, A., de Smedt, F., 2004. Modeling of a groundwater mound resulting from artificial recharge in the Gaza Strip, Palestine. In: Water for life in the Middle East, 2nd Israeli-Palestinian international conference, Turkey, 10-14 October.

Aris, R., 1956. On the Dispersion of a Solute by Diffusion, Convection and Exchange between Phases. Proc R Soc Lond 252 (1271), 538–550.

Arya, L. M., Paris, J. F., 1981. A Physicoempirical Model to Predict the Soil Moisture Characteristic from Particle-Size Distribution and Bulk Density Data. Soil Science Society of America Journal 45 (6), 1023–1030.

Atkinson, T. C., Oct. 1977. Diffuse flow and conduit flow in limestone terrain in the Mendip Hills, Somerset (Great Britain). Journal of Hydrology 35, 93–110.

Bear, J., 1972. Dynamics of fluids in porous media. Elsevier, New York.

Bear, J., 1979. Hydraulics of groundwater. McGraw-Hill International Book Co.

Benson, D. A., C. Tadjeran, M. M. Meerschaert, I. Farnham, and G. Pohll (2004). Radial fractional-order dispersion through fractured rock, Water Resour. Res., 40.

Chen, J.-S., Liu, C.-W., Hsu, H.-T., Liao, C.-M., Aug. 2003. A Laplace transform power series solution for solute transport in a convergent flow field with scale?dependent dispersion. Water Resources Research 39 (8).

Chesnaux, R., Mar. 2009. How groundwater seepage and transport modelling software can be useful for studying gaseous transport in an unsaturated soil. Water and Environment Journal 23 (1), 32–40.

Coppola, A., Basile, A., Comegna, A., Lamaddalena, N., Feb. 2009. Monte Carlo analysis of field water flow comparing uni- and bimodal effective hydraulic parameters for structured soil. Journal of Contaminant Hydrology 104 (14), 153–165.

Dagan, G., 1984. Solute transport in heterogeneous porous formations. Journal of Fluid Mechanics 145, 151–177.

Dagan, G., 1989. Flow and transport in porous formations., xvii + 465 pp.

Delin, G. N., Healy, R. W., Lorenz, D. L., Nimmo, J. R., Feb. 2007. Comparison of local- to regional-scale estimates of ground-water recharge in Minnesota, USA. Journal of Hydrology 334 (12), 231–249.

Fernandez-Garcia, D., Illangasekare, T. H., Rajaram, H., 2004. Conservative and sorptive forced-gradient and uniform flow tracer tests in a three-dimensional laboratory test aquifer. Water Resources Research 40, W10103.

Fiori, A., Jankovic, I., Dagan, G., 2006. Modeling flow and transport in highly heterogeneous three-dimensional aquifers: Ergodicity, Gaussianity, and anomalous behavior-2. Approximate semianalytical solution. Water Resources Research 42, W06D13.

Fiori, A., Zarlenga, A., Gotovac, H., Jankovic, I., Volpi, E., Cvetkovic, V., Dagan, G., Dec. 2015. Advective transport in heterogeneous aquifers: Are proxy models predictive? Water Resources Research 51 (12), 9577–9594.

Gelhar, L. W., Axness, C. L., 1983. Three-dimensional stochastic analysis of macrodispersion in aquifers. Water Resources Research 19 (1), 161–180.

Giddings, J. C., Dec. 1963. Kinetic Origin of Tailing in Chromatography. Analytical Chemistry 35 (13), 1999–2002.

Green, R. E., Corey, J. C., 1971. Calculation of Hydraulic Conductivity: A further Evaluation of some Predictive Methods1. Soil Sci. Soc. Am. J. 35 (5), 3–8.

Haggerty, R., Gorelick, S. M., 1995. Multiple-Rate Mass Transfer for Modeling Diffusion and Surface Reactions in Media with Pore-Scale Heterogeneity. Water Resources Research 31 (10), 2383–2400.

Hare, P. W., Morse, R. E., Jul. 1997. Water-Level Fluctuations Due to Barometric Pressure Changes in an Isolated Portion of an Unconfined Aquifer. Ground Water 35 (4), 667–671.

Hernandez-Coronado, H., Coronado, M., Herrera-Hernandez, E. C., Jun. 2012. Transport in fractal media: An effective scale-invariant approach. Physical Review E 85 (6), 66316.

Hughes, C. E., Binning, P., Willgoose, G. R., Nov. 1998. Characterisation of the hydrology of an estuarine wetland. Journal of Hydrology 211 (14), 34–49.

Joshi, N., Ojha, C. S. P., Sharma, P. K., Madramootoo, C. A., Jan. 2015. Application of nonequilibrium fracture matrix model in simulating reactive contaminant transport through fractured porous media. Water Resources Research 51 (1), 390–408.

Liu, Y., Kuang, X., Jiao, J. J., Li, J., Nov. 2015. Numerical study of variable-density flow and transport in unsaturatedsaturated porous media. Journal of Contaminant Hydrology 182, 117–130.

Masetti, M., Diolaiuti, G., D'Agata, C., Smiraglia, C., Jun. 2010. Hydrological Characterization of an Ice-Contact Lake: Miage Lake (Monte Bianco, Italy). Water Resources Management 24 (8), 1677–1696.

Masetti, M., Pedretti, D., Sorichetta, A., Stevenazzi, S., Bacci, F., Oct. 2015. Impact of a Storm-Water Infiltration Basin on the Recharge Dynamics in a Highly Permeable Aquifer. Water Resources Management, 1–17.

Matheron, G., 1967. Elements Pour Une Theorie des Milieux Poreux. Masson et Cie, Paris.

Molinari, A., Pedretti, D., Fallico, C., Jun. 2015. Analysis of convergent flow tracer tests in a heterogeneous sandy box with connected gravel channels. Water Resources Research, n/a–n/a.

Motha, J. A., Wigham, J. M., Jul. 1995. Modelling overland flow with seepage. Journal of Hydrology 169 (14), 265–280.

Neuman, S. P., Tartakovsky, D. M., 2009. Perspective on theories of non-Fickian trasport in heterogeneous media. Advances in Water Resources 32, 670–680.

Padilla, I. Y., Yeh, T.-C. J., Conklin, M. H., Nov. 1999. The effect of water content on solute transport in unsaturated porous media. Water Resources Research 35 (11), 3303–3313.

Pedretti, D., Fernandez-Garcia, D., Bolster, D.,Sanchez-Vila, X., 2013. On the formation of breakthrough curves tailing during convergent flow tracer tests in three-dimensional heterogeneous aquifers. Water Resources Research 49 (7), 4157–4173.

Pedretti, D., Fernandez-Garcia, D., Sanchez-Vila, X., Bolster, D., Benson, D. A., Feb. 2014. Apparent directional mass-transfer capacity coefficients in three-dimensional anisotropic heterogeneous aquifers under radial convergent transport. Water Resources Research 50 (2), 1205–1224.

Pedretti, D., Fiori, A., Oct. 2013. Travel time distributions under convergent radial flow in heterogeneous formations: Insight from the analytical solution of a stratified model. Advances in Water Resources 60, 100–109.

Pedretti, D., Masetti, M., Beretta, G. P., Vitiello, M., 2013. A Revised Conceptual Model to Reproduce the Distribution of Chlorinated Solvents in the Rho Aquifer (Italy). Groundwater Monitoring & Remediation 33 (3), 69–77.

Ptak, T., Piepenbrink, M., Martac, E., Jul. 2004. Tracer tests for the investigation of heterogeneous porous media and stochastic modelling of flow and transporta review of some recent developments. Journal of Hydrology 294 (13), 122–163.

Quilty, E. G., Roeloffs, E. A., Apr. 1997. Water-level changes in response to the 20 December 1994 earthquake near Parkfield, California. Bulletin of the Seismological Society of America 87 (2), 310–317.

Rolle M., Chiogna G. , Hochstetler, DL and Kitanidis, PK On the importance of diffusion and compound-specific mixing for groundwater transport: An investigation from pore to field scale. Journal of Contaminant Hydrology 153, 51–68

Saffman, P. G., 1960. Dispersion due to molecular diffusion and macroscopic mixing in flow through a network of capillaries. J. Flud Mech 2, 194–208.

Sauty, J. P., Oct. 1978. Identification des paramtres du transport hydrodispersif dans les aquifres par interprtation de traages en coulement cylindrique convergent ou divergent. Journal of Hydrology 39 (12), 69–103.

Sayana, V. B. M., Arunbabu, E., Kumar, L. M., Ravichandran, S., Karunakaran, K., Feb. 2010. Groundwater Responses to Artificial Recharge of Rainwater in Chennai, India: a Case Study in an Educational Institution Campus. Indian Journal of Science and Technology 3 (2), 124–130.

Schulze-Makuch, D., May 2005. Longitudinal dispersivity data and implications for scaling behavior. Groundwater 43 (3), 443–456.

Simpson, B., Blower, T., Craig, R. N., Wilkinson, W. B., 1989. The engineering implications of rising groundwater levels in the deep aquifer beneath London. CIRIA Special Publication (69).

Valocchi, A. J., Nov. 1986. Effect of radial flow on deviations from local equilibrium during sorbing solute transport through homogeneous soils. Water Resources Research 22 (12), 1693–1701.

van Genuchten, M. T., Wierenga, P. J., 1976. Mass Transfer Studies in Sorbing Porous Media I. Analytical Solutions. Soil Science Society of America Journal 40 (4), 473.

Vishal, V., Leung, J. Y., Nov. 2015. Modeling impacts of subscale heterogeneities on dispersive solute transport in subsurface systems. Journal of Contaminant Hydrology 182, 63–77.

Woesten, J. H. M., van Genuchten, M. T., 1988. Using Texture and Other Soil Properties to Predict the Unsaturated Soil Hydraulic Functions. Soil Science Society of America Journal 52 (6), 1762.

Zhang, Y., Green, C. T., Tick, G. R., Jun. 2015. Peclet number as affected by molecular diffusion controls transient anomalous transport in alluvial aquiferaquitard complexes. Journal of Contaminant Hydrology 177178, 220–238.

Figure 1

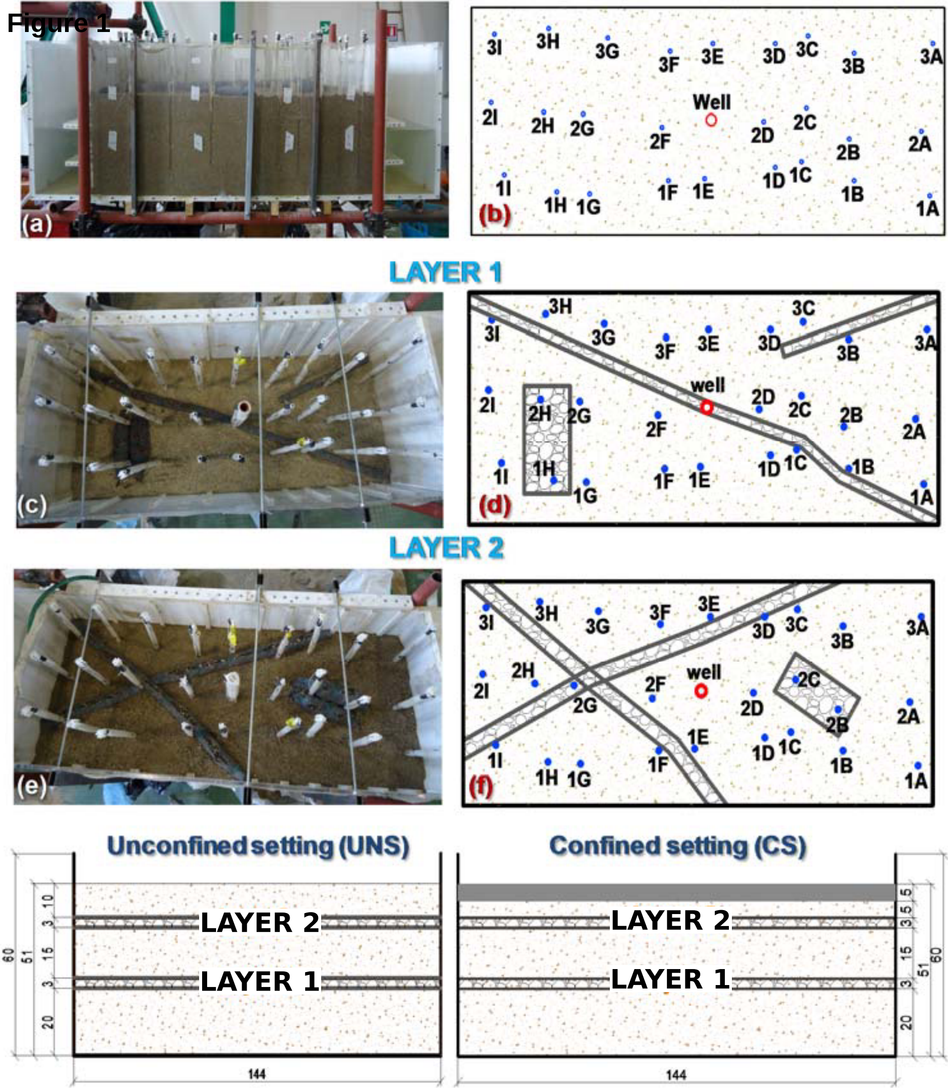
(a)
(b)
3I 3H 3G 3F 3E 3D 3C 3B 3A
Well
2I 2H 2G 2F 2D 2C 2B 2A
1I 1H 1G 1F 1E 1D 1C 1B 1A
LAYER 1
(c)
(d)
well
LAYER 2
(e)
(f)
Unconfined setting (UNS)
Confined setting (CS)
LAYER 2
LAYER 1
10
3
15
3
20
51
60
5
3.5
144

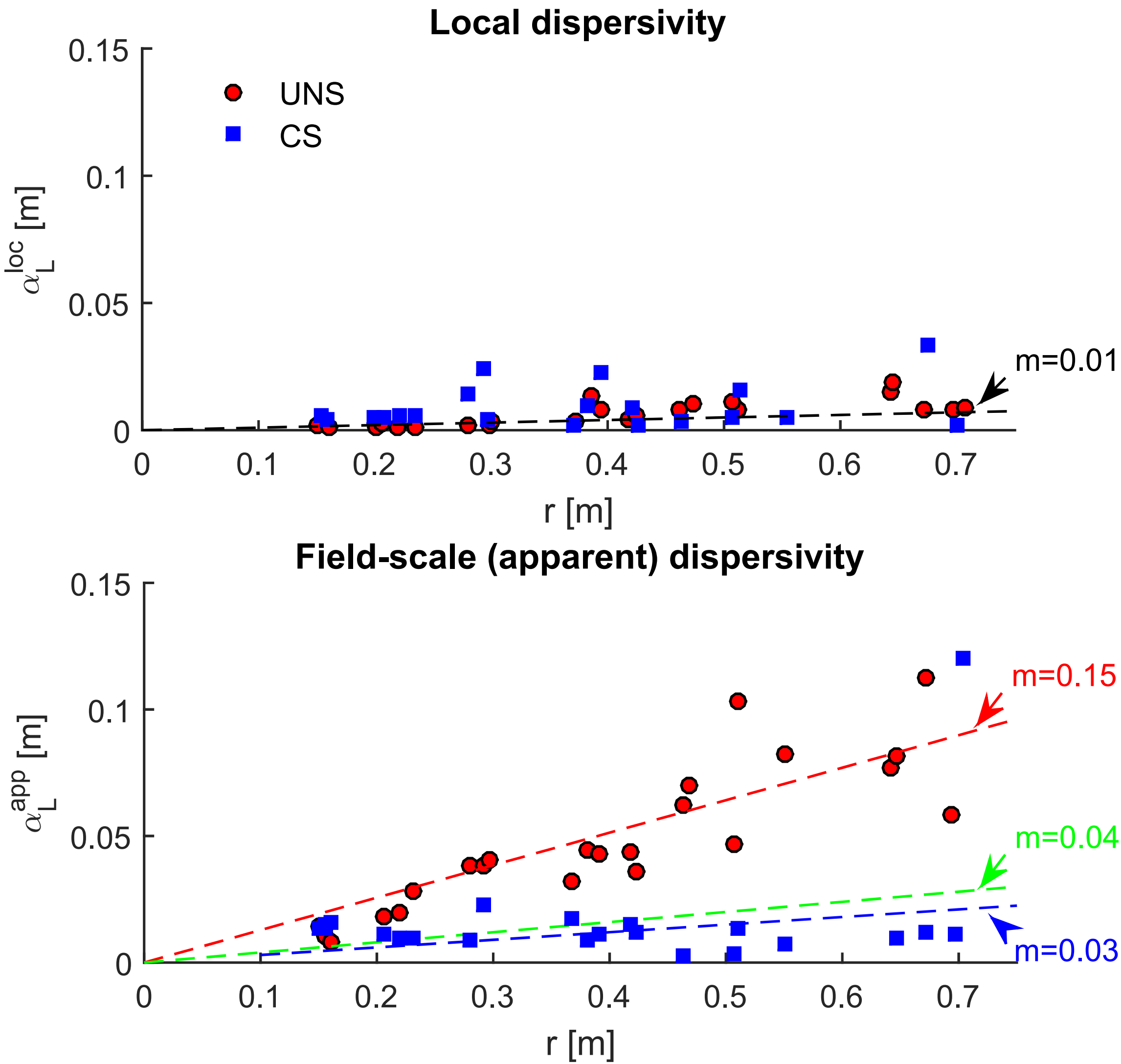

Local dispersivity
UNS
CS
α_L^{loc} [m]
0.15
0.1
0.05
0
0
0.1
0.2
0.3
0.4
0.5
0.6
0.7
r [m]
m=0.01
Field-scale (apparent) dispersivity
α_L^{app} [m]
0.15
0.1
0.05
0
0
0.1
0.2
0.3
0.4
0.5
0.6
0.7
r [m]
m=0.15
m=0.04
m=0.03

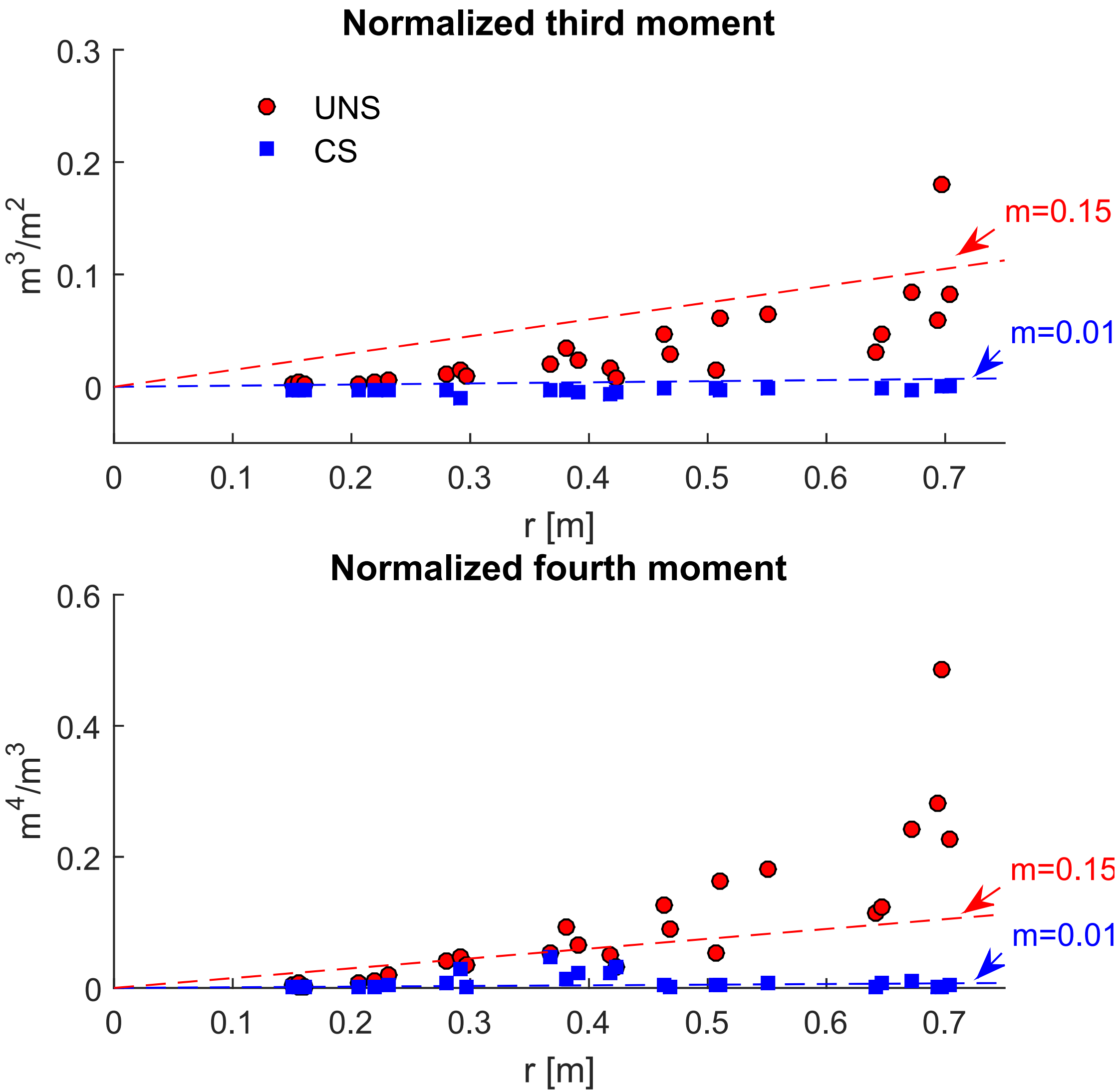

Normalized third moment
0.3
0.2
0.1
0
m^3/m^2
UNS
CS
m=0.15
m=0.01
0
0.1
0.2
0.3
0.4
0.5
0.6
0.7
r [m]
Normalized fourth moment
0.6
0.4
0.2
0
m^4/m^3
m=0.15
m=0.01
0
0.1
0.2
0.3
0.4
0.5
0.6
0.7
r [m]

Figure 4

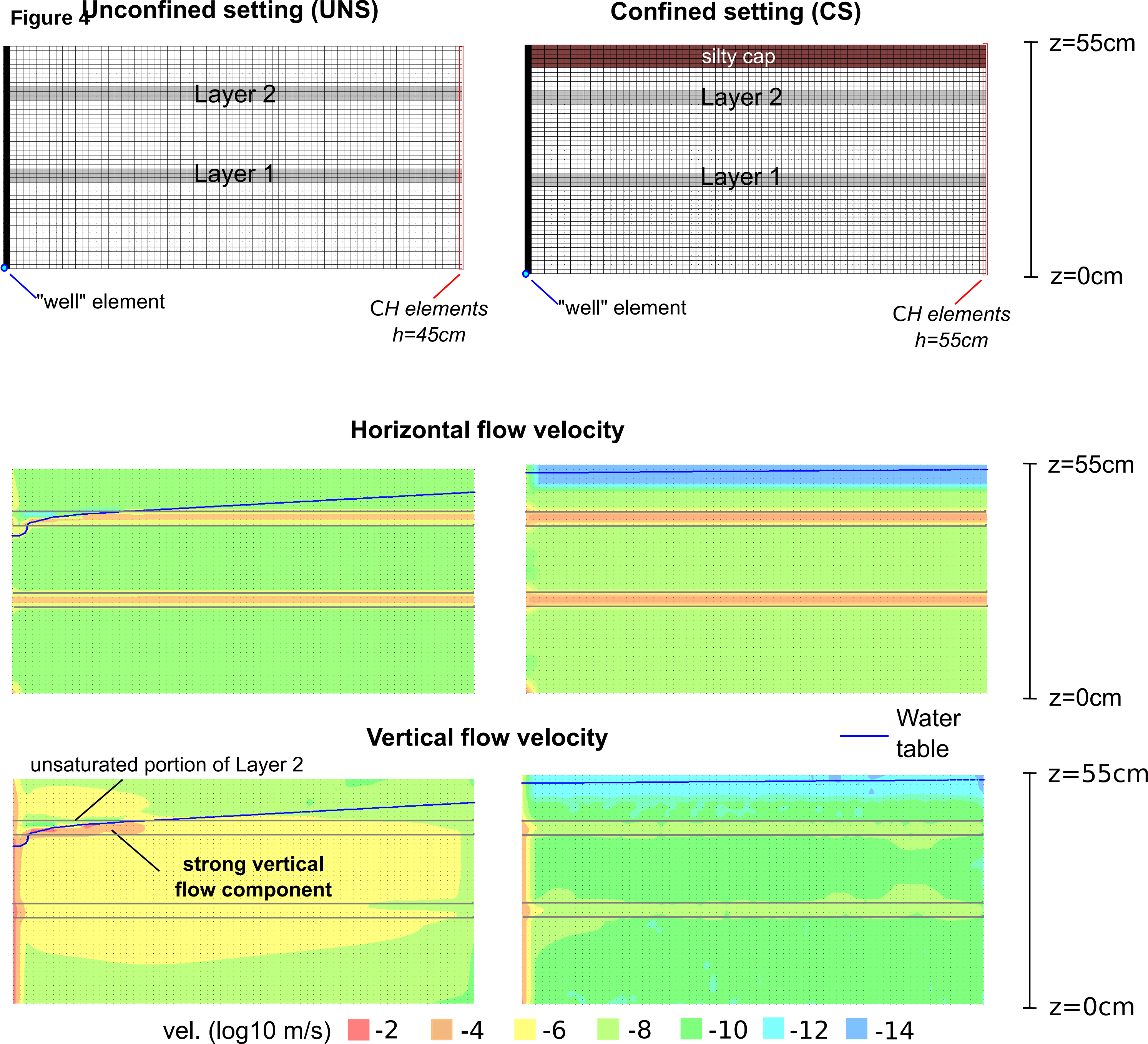

Unconfined setting (UNS)
Confined setting (CS)
silty cap
Layer 2
Layer 1
Layer 2
Layer 1
"well" element
CH elements
h=45cm
"well" element
CH elements
h=55cm
z=55cm
z=0cm
Horizontal flow velocity
z=55cm
z=0cm
Vertical flow velocity
Water
table
unsaturated portion of Layer 2
strong vertical
flow component
z=55cm
z=0cm
vel. (log10 m/s)
-2
-4
-6
-8
-10
-12
-14

Figure 5

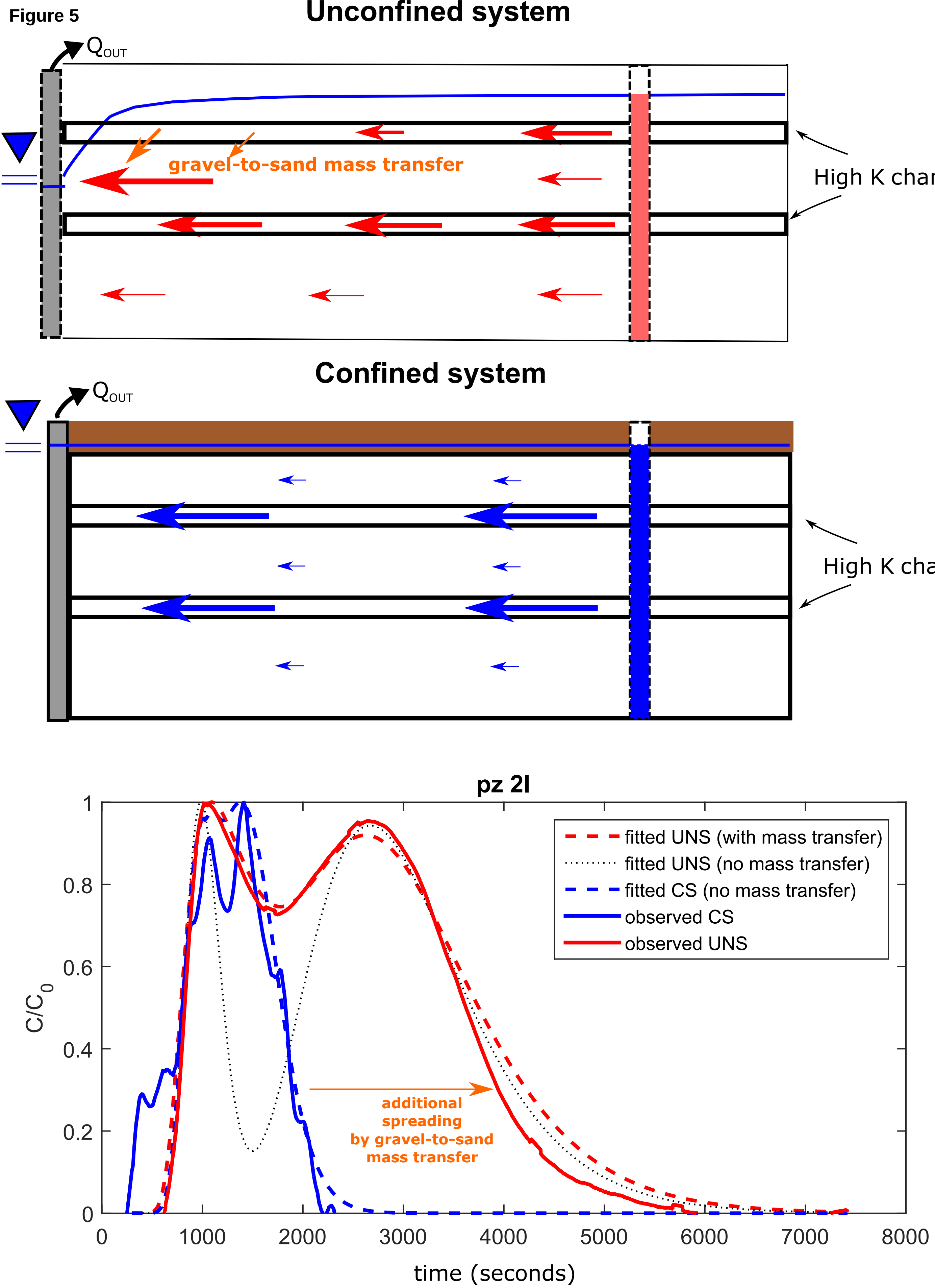

Unconfined system
Q_{OUT}
gravel-to-sand mass transfer
High K channels
Confined system
Q_{OUT}
High K channels
pz 2I
fitted UNS (with mass transfer)
fitted UNS (no mass transfer)
fitted CS (no mass transfer)
observed CS
observed UNS
additional spreading by gravel-to-sand mass transfer
C/C0
time (seconds)
0
0.2
0.4
0.6
0.8
1
0
1000
2000
3000
4000
5000
6000
7000
8000